Article

Linking oxidative and reductive clusters to prepare crystalline porous catalysts for photocatalytic CO$_2$ reduction with H$_2$O

Jie Zhou[1,2], Jie Li[1,2], Liang Kan[1], Lei Zhang[1], Qing Huang[1], Yong Yan [1]✉, Yifa Chen [1], Jiang Liu [1], Shun-Li Li[1] & Ya-Qian Lan [1]✉

Mimicking natural photosynthesis to convert CO$_2$ with H$_2$O into value-added fuels achieving overall reaction is a promising way to reduce the atmospheric CO$_2$ level. Casting the catalyst of two or more catalytic sites with rapid electron transfer and interaction may be an effective strategy for coupling photocatalytic CO$_2$ reduction and H$_2$O oxidation. Herein, based on the MOF ∪ COF collaboration, we have carefully designed and synthesized a crystalline heterometallic cluster catalyst denoted MCOF-Ti$_6$Cu$_3$ with spatial separation and functional cooperation between oxidative and reductive clusters. It utilizes dynamic covalent bonds between clusters to promote photo-induced charge separation and transfer efficiency, to drive both the photocatalytic oxidative and reductive reactions. MCOF-Ti$_6$Cu$_3$ exhibits fine activity in the conversion of CO$_2$ with water into HCOOH (169.8 μmol g^{-1}h^{-1}). Remarkably, experiments and theoretical calculations reveal that photo-excited electrons are transferred from Ti to Cu, indicating that the Cu cluster is the catalytic reduction center.

Converting CO$_2$ and H$_2$O with solar energy into carbon-based fuels is a potential solution that could solve the problems of global warming and energy supply, which is in line with the global green and low-carbon development strategy[1–4]. However, there is still a long way to realize photocatalytic overall oxidative and reductive reactions, due to the inability of fast photogenerated electron-hole pairs recombination to satisfy both the kinetics of overcoming the high chemical inertness of CO$_2$ molecules and the slow oxidation of water[5–9]. In nature, the chlorophyll aggregate P680 of green plants captures light energy for charge separation, then pheophytin pigment rapidly captures electrons to produce the radical cation P680$^+$, providing separated electron-hole to complete the conversion of CO$_2$ and H$_2$O into carbon-based fuels[10–13]. Up to date, tremendous efforts have been made to mimic green plants, including type II and Z-scheme heterojunctions for the artificial photosynthesis systems[14–17]. Therefore, combining two or more catalytic sites to accomplish spatial separation of oxidative and reductive centers, rapid transfer of electrons, and functional

interactions may be a promising strategy for realizing the overall photoreaction[18–20]. Nevertheless, cumbersome synthetic procedures and loss of atomic-scale control are the serious flaws of these strategies, which hinder the understanding of photocatalysis at the atomic level[21,22].

The reticular crystalline materials, metal organic frameworks (MOFs) and covalent organic frameworks (COFs), have made great potential in photocatalytic CO$_2$ conversion, a frontier in the study of structure-property correlations constructed on the atomic level[23–27]. However, the difficulty to accurately control the structure of the framework material with dual active sites in the in-situ synthesis of crystalline materials may restrict their further development in the conversion of CO$_2$. Exploring metal clusters or molecular complexes with defined composition and directionality linked with other metal complexes by coordination linkages or even dynamic covalent linkages might be a promising avenue to overcome these shortcomings[28]. To date, the active sites of oxidative or reductive reactions are only

[1]School of Chemistry, South China Normal University, Guangzhou 510006, P.R. China. [2]These authors contributed equally: Jie Zhou, Jie Li.
✉e-mail: Yong.Yan@m.scnu.edu.cn; yqlan@m.scnu.edu.cn

found on a single species (oxidative or reductive homo-metallic clusters) in the reported examples, which is unfavorable for completing the artificial photosynthetic overall reaction[29–32]. If the clusters with water oxidative ability and CO_2 reductive ability can be connected, it is possible to realize the overall reaction of artificial photosynthesis without additional photosensitizers and sacrificial agents[9,14]. Currently, the mainstream methods to achieve the incorporation of dual active sites with different functions in one single material are by integrating photoactive centers into the structure[33] or post synthetic modification[20,34], albeit with some issues, such as cumbersome synthesis and product uncertainty. Therefore, directionally assembling two different clusters with oxidative and reductive abilities via covalent bonds for preparing crystalline porous catalysts may be a brand-new strategy for artificial photosynthesis[35–39]. Due to the stability and solubility issues of different clusters during synthesis and crystallization, almost no reports have been published to realize the construction of cluster-based crystalline porous catalysts through the linkage by covalent bonds.

With the above in mind, to complete the overall reaction directly, a hetero-metallic cluster catalyst, namely MCOF-Ti_6Cu_3, has been intentionally constructed with Ti-O clusters with oxidation ability[40,41] and Cu clusters with reduction capacity[42,43] for effective coupling photocatalytic CO_2 reduction and H_2O oxidation. MCOF-Ti_6Cu_3 was prepared by directed assembly through relatively mild dynamic covalent linkages, enabling both rapid electron transfer and synergistic interactions between clusters, without damaging the intrinsic individual components and preserving their oxidative and reductive properties. Under simulated sunlight irradiation, MCOF-Ti_6Cu_3 exhibited excellent photocatalytic activity in the generation of HCOOH with a yield of 20.39 μmol in 12 h with O_2 release, at a high level among the reported non-noble metal photocatalysts with overall reaction. The existence of an internal electric field in MCOF-Ti_6Cu_3 with the Ti cluster

pointing to the Cu cluster was confirmed by X-ray photoelectron spectroscopy (XPS). Notably, the in-situ XPS and density functional theory (DFT) calculations proved that electrons reach to the Cu cluster under light excitation conditions, and finally the reductive reaction occurs at the Cu cluster and the oxidative reaction at the Ti cluster, which is consistent with the oxidative and reductive centers of the pre-designed material. Finally, in-situ diffuse reflectance infrared Fourier transform spectroscopy (DRIFTS) and DFT calculations unambiguously unveiled the intermediates and mechanism of the photoreaction. This work not only provides a rational strategy for constructing hetero-metallic cluster catalyst, but also an insight into photocatalytic overall reaction by using accurate structural models. Overall, our findings may shed light on the application of crystalline materials in the field of photocatalytic overall reaction for CO_2 and H_2O conversion.

Results and discussion

Two precursors $[Ti_6O_6(O^iPr)_6(AB)_6]$ (AB = 4-aminobenzoate; HO^iPr = isopropoxide, denoted **Ti_6**)[44] and $[Cu_3(PyCA)_3]$ (1H-PyCA = pyrazolate-4-carboxaldehyde, denoted **Cu_3**)[32] were prepared according to the previously reported methods. The synthesis of MCOF-Ti_6Cu_3 was carried out from the condensation of **Ti_6** and **Cu_3** in a mixture of mesitylene and N, N-Dimethylformamide (DMF) under the vacuum solvothermal conditions (Fig. 1a). Fourier-transform infrared (FT-IR) spectra confirmed the condensation reaction between the two starting materials by the obvious disappearance of the C = O (1685 cm^{-1}) and N-H (3200–3500 cm^{-1}) stretching vibration peaks found in **Cu_3** and **Ti_6**, respectively (Fig. 1b). In addition, a new characteristic peak at 1625 cm^{-1} attributed to the C = N bond was observed, indicating the successful formation of an imine-linked network[45]. Powder X-ray diffraction (PXRD) pattern of MCOF-Ti_6Cu_3 displayed the strongest diffraction peak at 2θ 6.1° corresponding to (110) reflection plane, along with minor peaks at 12.4°, 18.8°, 20.4°, and 25.3° that are attributed to the
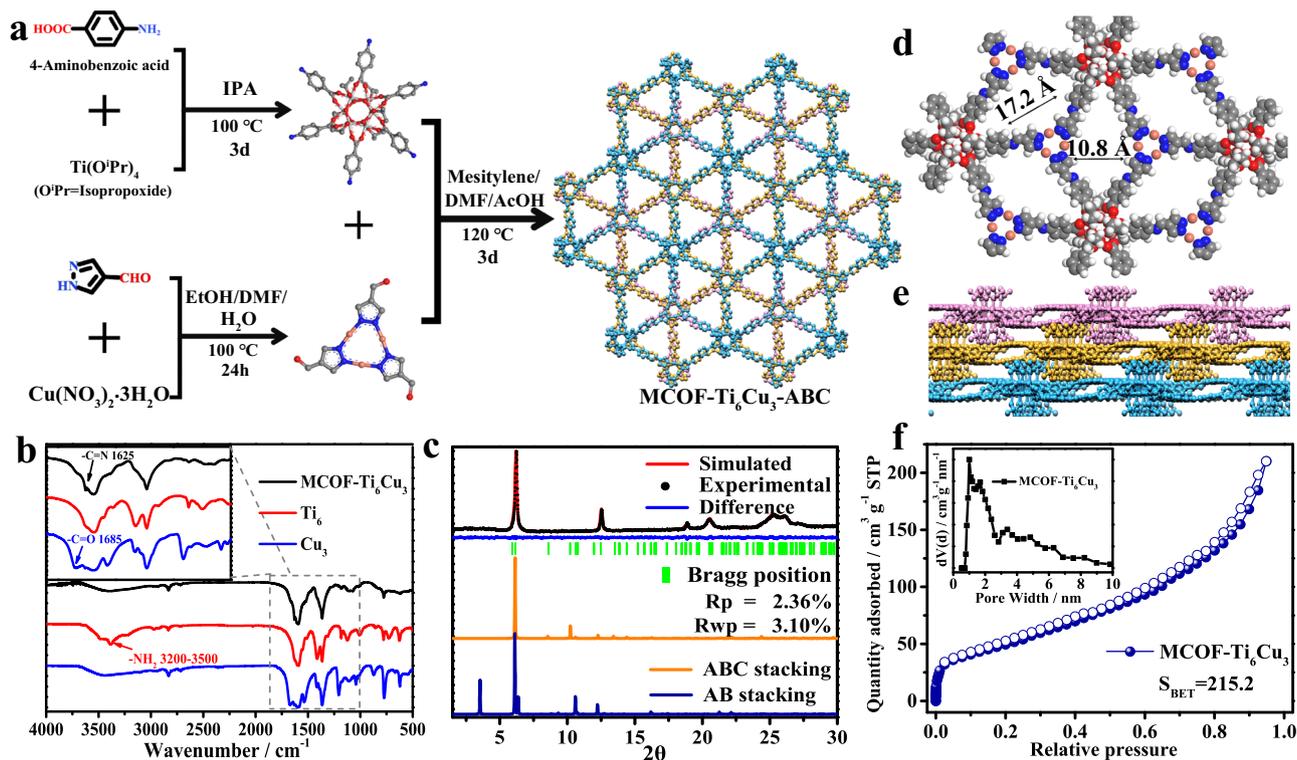
Fig. 1 | The preparation and characterization. a Schematic of the synthesis of MCOF-Ti_6Cu_3 via the condensation of **Ti_6** and **Cu_3**. **b** IR spectra of MCOF-Ti_6Cu_3, **Ti_6** and **Cu_3**. **c** Experimental and simulated PXRD patterns of MCOF-Ti_6Cu_3. **d** Top and **e** side views of the structure of MCOF-Ti_6Cu_3. Atomic color: Carbon (gray), Nitrogen (blue), Oxygen (red), Copper (orange), Titanium (silver) and Hydrogen (white) **f** N_2 adsorption curve of MCOF-Ti_6Cu_3 at 77 K (inset shows the pore-size distribution profile).
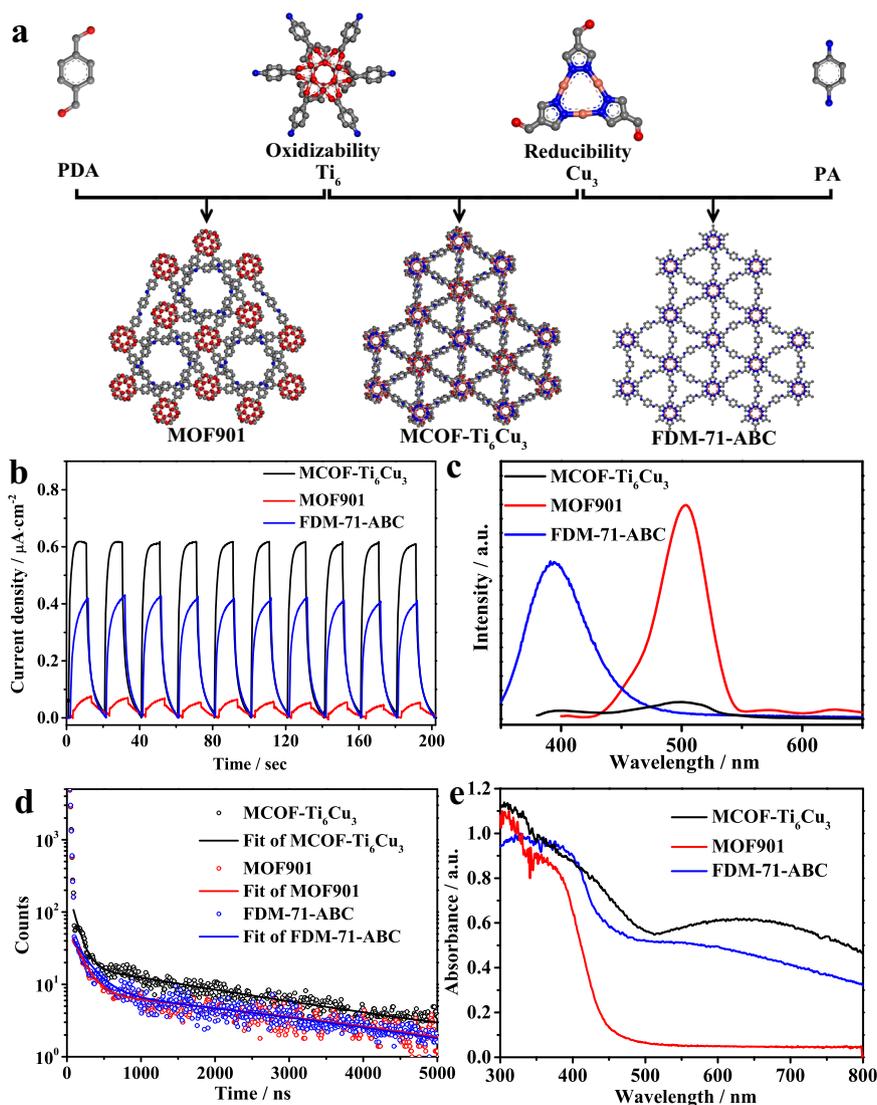
**Fig. 2 | Comparisons for photochemical properties. a** Schematic of the synthesis of MOF901, FDM-71-ABC, and MCOF-Ti$_6$Cu$_3$. Photoelectrical Properties of MOF901, FDM-71-ABC, and MCOF-Ti$_6$Cu$_3$: **b** Transient photocurrent responses. **c** Steady-state PL spectra. **d** Transient PL decay. **e** The solid-state UV-vis DRS.

(220), (330), (502), and (440) crystal planes, respectively (Fig. 1c). To elucidate the crystal structure of MCOF-Ti$_6$Cu$_3$, the staggered stacking model in the R_3 and P_{63} space groups corresponding to ABC and AB stacking were built using Materials Studio[28,31,46]. The experimental PXRD pattern matches well with the simulated one for the ABC stacking model. Pawley refinement was applied to provide the refined unit cell parameters of $a = b = 29.14$ Å, $c = 18.97$ Å, with good residual factors of $R_p = 2.36\%$ and $R_{wp} = 3.10\%$, suggesting the validity of the computational model. The structural information for the AB stacking model is in the Supplementary Information.

These structural analyses reveal that a rhombic channel along c axis with a theoretical pore size of 1.08 nm × 1.72 nm and interlayer distance of 5.6 Å (Fig. 1d, e). The porosity and surface area of MCOF-Ti$_6$Cu$_3$ were examined by N$_2$ adsorption-desorption measurements at 77 K (Fig. 1f). The Brunauer-Emmett-Teller (BET) surface area was calculated to be 215.2 m^2 g^{-1}. Besides, the pore size distribution (~1.01 and ~1.68 nm) of MCOF-Ti$_6$Cu$_3$ were in good agreement with the results predicted from the theoretical structure model. The crystallinity and structure of MCOF-Ti$_6$Cu$_3$ remained by treating it with various solvents at room temperature, which was confirmed by PXRD analyses (Supplementary Fig. 9). The thermal stability of MCOF-Ti$_6$Cu$_3$ was confirmed by thermogravimetric analysis (TGA) (Supplementary Figs. 10,

11, and 12), which showed no noticeable weight loss up to 300 °C. The morphology of MCOF-Ti$_6$Cu$_3$ was characterized by scanning electron microscopy (SEM) and transmission electron microscopy (TEM). The SEM and TEM images of MCOF-Ti$_6$Cu$_3$ shown in Supplementary Figs. 13 and 14 display a sheet-like morphology, which is apparently different from the regular octahedral structure of **Ti$_6$** (Supplementary Fig. 15) and the needle-shaped particles of **Cu$_3$** (Supplementary Fig. 16). In addition, the high-resolution TEM (HRTEM) image distinctly reveals the high crystallinity of MCOF-Ti$_6$Cu$_3$ (Supplementary Fig. 17). The corresponding energy-dispersive X-ray spectroscopy (EDS) mapping spectra (Supplementary Fig. 18) indicate that Ti and Cu elements are uniformly distributed in MCOF-Ti$_6$Cu$_3$.

In order to conduct a more in-depth study on the hetero-metallic cluster catalyst of MCOF-Ti$_6$Cu$_3$, we also analyzed two monometallic cluster framework materials named MOF901[28] and FDM-71-ABC[32] as control samples, which were synthesized from **Ti$_6$** with *p*-benzaldehyde and **Cu$_3$** with *p*-phenylenediamine, respectively (Fig. 2a, see Supplementary Information for details). For photocatalytic reduction of CO$_2$, the separation and migration behavior of photogenerated electron-hole pairs is one of the critical factors. The photoelectro-chemical properties of the samples were performed with the combination of transient photocurrent
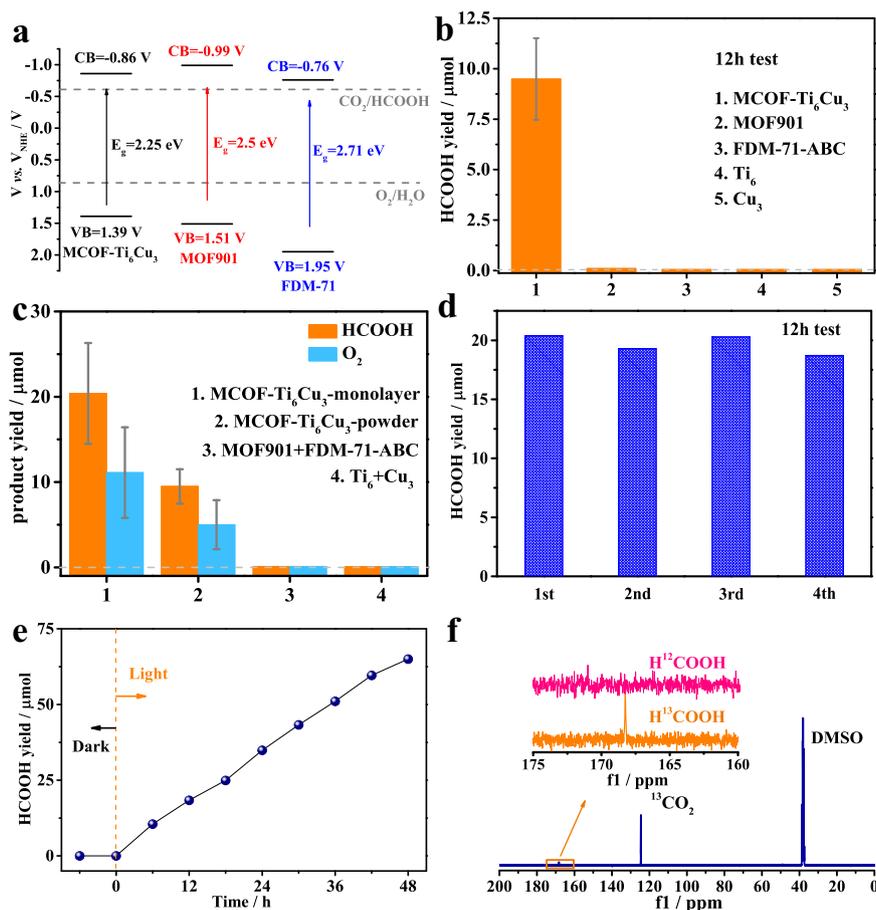
Fig. 3 | The CO_2RR performance for various photocatalysts. a Band structure diagram of MOF901, FDM-71-ABC and MCOF-Ti_6Cu_3. Photocatalysis performances: **b** The comparison of HCOOH yields for different samples. **c** The photocatalytic products yields for samples with different morphology and physical mixtures. **d** Durability measurements (12 h test per cycle). **e** Time-dependent HCOOH production. **f** ^{13}C NMR spectra for the photocatalytic reaction solution from $^{13}CO_2$ atmosphere. The error bar represents the standard deviation of the measurements.

measurements, electrochemical impedance spectroscopy (EIS) and photoluminescence (PL) spectra. Figure 2b shows that all samples exhibit obvious photocurrent signals and have an excellent reproducibility of the response intensity in the process of on-off cycles. The transient photocurrent intensity of MCOF-Ti_6Cu_3 is ~1.5 times that of FDM-71-ABC and much higher than that of MOF901. Moreover, the photocurrent intensity of **Cu_3** is about three times as high as **Ti_6**, indicating that the **Cu_3** cluster may have better photosensitivity (Supplementary Fig. 19). The EIS spectra reveal that compared with MOF901 and FDM-71-ABC, MCOF-Ti_6Cu_3 exhibits a smaller semicircle radius in the high-frequency region in Nyquist plots, suggesting a higher separation and transfer efficiency of charge carriers in MCOF-Ti_6Cu_3 (Supplementary Fig. 20). As presented in Fig. 2c, the spectral peak position of FDM-71-ABC which originates from **Cu_3** cluster (Supplementary Fig. 21) is about 400 nm[32], while that of MOF901 which originates from **Ti_6** cluster (Supplementary Fig. 22) is about 500 nm[28]. In contrast, MCOF-Ti_6Cu_3 exhibits two shifted peaks with the weakest PL intensity, indicating the existence of electron transfer and the lowest recombination efficiency of photoinduced electron-hole pairs. Meanwhile, time-resolved fluorescence decay spectra were measured to determine the specific charge carrier dynamics (Fig. 2d). The results showed that the average lifetime of the photogenerated charge carriers in MCOF-Ti_6Cu_3 was 1.90 ± 0.26 μs, which is comparable to that of FDM-71-ABC (1.67 ± 0.09 μs) and longer than that of MOF901 (1.28 ± 0.15 μs). The difference of fluorescence lifetime between MCOF-Ti_6Cu_3 and FDM-71-ABC can also be directly evident

from the fluorescence decay data (Fig. 2d), which shows that the fluorescence decays with a lower rate in MCOF-Ti_6Cu_3 compared with those in the other two samples, illustrating that the photogenerated charge carriers survived longer on the surface of MCOF-Ti_6Cu_3. These results further demonstrate that the spatially separated hetero-metallic cluster structures can effectively capture photogenerated electrons and holes respectively, reduce the change of recombination of charge carriers and facilitate their separation and migration in the framework in favor of the higher photocatalytic activity.

The solid-state UV-vis diffuse reflectance spectra (UV-vis DRS) of the samples were recorded. As shown in Fig. 2e, FDM-71-ABC and MCOF-Ti_6Cu_3 exhibited considerable absorption in the UV and visible regions, whereas the absorption edge of MOF901 was only located near 650 nm. Evaluated by the Tauc plots, the corresponding band gap energies (E_g) of MOF901, FDM-71-ABC, and MCOF-Ti_6Cu_3 were calculated to be 2.5, 2.71, and 2.25 eV, respectively (Supplementary Figs. 23, 24 and 25). Furthermore, Mott-Schottky measurements were performed to elucidate the semiconductor character of the samples (Supplementary Figs. 26, 27 and 28). The flat band potentials of MOF901, FDM-71-ABC, and MCOF-Ti_6Cu_3 were determined to be −1.06, −1.19, and −0.96 V vs. Ag/AgCl (i.e., −0.86, −0.99, and −0.76 V vs. NHE), respectively, which are equal to their conduction band (CB) potentials[47]. Based on the equation $E_g = E_{VB} - E_{CB}$, their valence band (VB) positions were accordingly calculated to be 1.39, 1.51, and 1.95 V vs. NHE, respectively (Fig. 3a). Considering the CB/VB and LUMO/HOMO, the energy of CB/VB is equivalent to the electrochemical

energy potentials of LUMO/HOMO. Obviously, they are thermo-dynamically suitable for photocatalytic reduction of CO_2 together with oxidation of H_2O to various fuels.

The simultaneous completion of CO_2 reduction and H_2O oxidation is a great challenge. Therefore, the performance of photo-catalytic reduction of CO_2 with H_2O over the samples was systematically investigated under simulated sunlight irradiation. As shown in Fig. 3b, the main product of the CO_2 photocatalytic reduction with MCOF-Ti_6Cu_3 was HCOOH, of which the yield reached 9.28 µmol (77.3 µmol g^{-1}h^{-1}) after 12 h illumination, while no gaseous products were detected, resulting in a high selectivity. In sharp contrast, MOF901 or FDM-71-ABC showed inactive for CO_2 reduction, indicating that neither Ti nor Cu cluster could complete the CO_2 reduction coupled with H_2O oxidation. In addition, control experiments with **Ti₆** and **Cu₃** as the photocatalysts for CO_2 reduction have also been evaluated under identical conditions. It cloud be found that no HCOOH was observed, indicating that neither the precursor nor homo-metallic cluster catalyst can complete the overall reaction alone. The PXRD pattern and FT-IR suggested structural integrity and no noticeable loss of crystallinity for MCOF-Ti_6Cu_3 after reactions, demonstrating its excellent stability (Supplementary Figs. 29 and 30).

The structural units of MCOF-Ti_6Cu_3 are clusters, in which interlayer spacing is larger than that of the traditional two-dimensional COFs. Therefore, stripping MCOF-Ti_6Cu_3 into single layers is feasible employing high-frequency ultrasound[48]. As shown in Supplementary Fig. 31, after dispersing 10 mg of MCOF-Ti_6Cu_3 into 30 mL of deionized water, the nanosheets with the thickness of 4.83 nm were obtained by high-frequency ultrasound for 30 min. The resulting nanosheet structure exhibited a dramatically enhanced yield of HCOOH to 20.39 µmol in 12 h (169.8 µmol g^{-1}h^{-1}) (Fig. 3c), which was superior to most of the previously reported noble-metal-free photocatalysts in overall reactions (Supplementary Table 5). Exfoliation has little effects on transient photocurrent responses and electrochemical impedance, but the gas adsorption and specific surface area were greatly improved (Supplementary Figs. 32, 33 and 34). The exfoliation exposes more adsorption sites and active centers, which may be the reason for the excellent photocatalytic performance. The physically mixed control experiments with **Ti₆** + **Cu₃** or MOF901 + FDM-71-ABC composites were performed. No products were detected, which demonstrates the necessity of the assembly of MCOF-Ti_6Cu_3 in the framework. In addition, in order to evaluate the catalytic stability and reusability of MCOF-Ti_6Cu_3, recycling experiments and long-term tests were carried out. As shown in Fig. 3d, MCOF-Ti_6Cu_3 retained the original photocatalytic efficiency for the HCOOH production during four consecutive cycles. MCOF-Ti_6Cu_3 nanosheets possessed excellent durability during the photocatalytic process, which was further confirmed by the time-dependent conversion yields of CO_2 into HCOOH, which gradually increased with time (Fig. 3e, Supplementary Fig. 35). The yield of products no longer increased after the removal of catalyst from the reaction, further ruling out the possibility of leaching of Ti and Cu (Supplementary Fig. 36).

Additional control experiments demonstrated that negligible reduction products could be detected without the photocatalyst, CO_2, or light irradiation. These results suggested that those factors were all indispensable for photocatalytic CO_2 reduction, and the generated HCOOH originated from CO_2 rather than the photolysis from other carbon-containing species in this photocatalytic system. In order to further verify the origin of HCOOH, the $^{13}CO_2$ isotope trace experiment was performed. The ^{13}C NMR spectrum gave the corresponding isotope H^{13}COOH signal with a peak at 168.4 ppm, and there was no such signal under the same condition as for $^{12}CO_2$ (Fig. 3f), unambiguously verifying that the carbon source of HCOOH indeed originated from the CO_2 reduction. Alternatively, when H_2O was replaced with $H_2^{18}O$, $^{18}O_2$

($m/z = 36$), $^{18}O^{16}O$ ($m/z = 34$) and $^{16}O_2$ ($m/z = 32$) were detected after the reaction, confirming that the generated $^{18}O_2$ or $^{16}O_2$ was from $H_2^{18}O$ or $H_2^{16}O$ (Supplementary Fig. 37)[45,49].

To investigate the mechanism of the photocatalytic overall reaction XPS and in-situ XPS measurements combined with DFT calculations (method in Supplementary Information) were carried out. The calculation model was constructed based on the finite cluster structure of MCOF-Ti_6Cu_3 (Supplementary Fig. 38). XPS showed that the observed Ti 2p binding energy at 459.0 eV in **Ti₆** was consistent with Ti^{4+}, while the Cu 2p binding energy at 932.8 eV and 934.6 eV in **Cu₃** were assigned to Cu^{1+} and Cu^{2+}, respectively (Fig. 4a, b)[18,30]. Previous studies found that the production of Cu^{2+} was due to the surface oxidation, and the Cu valence could be switched between Cu^{1+} and Cu^{2+} without altering the backbone of Cu_3(pyrazolate)$_3$ triangular SBUs[32,50]. For MCOF-Ti_6Cu_3, the negative shift of the Ti 2p binding energy by 0.4 eV and the positive shift of the Cu 2p binding energy by 0.7 eV indicated a successful covalent-bond connection between the two precursors with the formation of an internal electric field, and the possible migration direction of electrons was from Cu to Ti. This interaction from cluster-to-cluster was conducive to the transfer of electrons. The XPS spectra of C, N and O elements are shown in Supplementary Figs. 39, 40 and 41.

The electron transfer process in the photocatalytic reaction could be distinctly revealed by the valence change using in-situ XPS measurements. As shown in Fig. 4c, d, under irradiation (black and red line), the Ti 2p binding energy increased from 458.46 eV to 458.61 eV. In comparison, the Cu 2p binding energy decreased from 932.94 eV to 932.78 eV, indicating that some electrons returned to Cu cluster with photoexcitation. After CO_2 was introduced into the system (red and blue line), the binding energy of Cu 2p increased to 932.94 eV while that of Ti 2p was unchanged, indicating that the transfer direction of the photogenerated electrons was from the Cu cluster to CO_2. Consequently, it could be inferred that the active center of the photocatalytic reduction of CO_2 to HCOOH over MCOF-Ti_6Cu_3 was the Cu cluster. Finally, as shown in the Supplementary Figs. 42, 43 and 44, the in-situ XPS and in-situ DRIFTS spectra before and after the reaction were consistent, which proves the good stability of the catalyst. As shown in electrostatic potential (ESP) analyses (Supplementary Fig. 45), the positive charge was concentrated on the Cu-N cluster and benzene moieties, while the negative charge was concentrated on the Ti-O cluster.

The DFT and time-dependent DFT (TDDFT) calculation results could also prove that the photocatalytic CO_2 reduction reaction on the Cu cluster in MCOF-Ti_6Cu_3[51,52]. The TDDFT calculation results (Supplementary Fig. 46) show that the HOMO and LUMO of MCOF-Ti_6Cu_3 are close to each other and can be excited by the excitation energy of infrared light (1704.16 nm). However, visible and ultraviolet lights correspond to multiple excitation modes. The visible lights with wavelengths of 487.42 nm and 453.25 nm corresponded to the excitation modes of HOMO → LUMO + 27, + 29, + 31, and HOMO → LUMO + 31, + 32, while the wavelengths of 352.79 nm and 351.89 nm in ultraviolet region correspond to the excitation modes of HOMO − 3 → LUMO + 1 and HOMO 1 → LUMO + 1, respectively. The orbital composition analysis displays that the occupied orbitals of HOMO, − 1, and − 3 are located on the Cu cluster fragments, and the unoccupied orbitals of LUMO, + 27, + 29, + 31, and + 32 are also located on the Cu cluster fragments, other unoccupied orbitals are located on the Ti cluster fragments. It demonstrates that the electron cloud does not transfer in the process of infrared excitation, and indeed transfers from the Cu cluster to the Ti cluster under ultraviolet excitation. The electron cloud is distributed on the Cu cluster under visible excitation, which corresponds to the result that the Cu cluster receives electrons under optical excitation from the in-situ XPS measurement.

To further clarify the reasons for the excellent photocatalytic activity and HCOOH conversion selectivity, in-situ DRIFTS
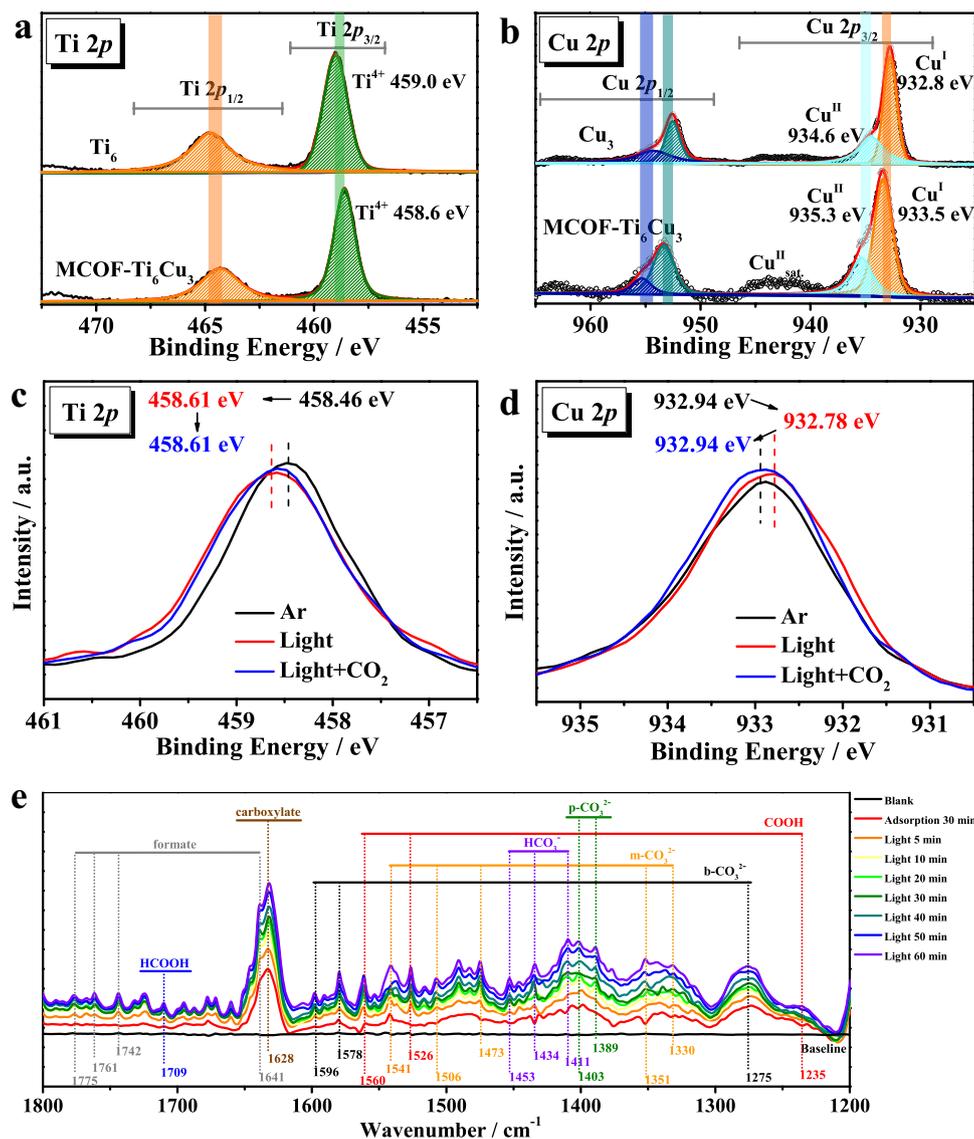
Fig. 4 | XPS and In-situ measurements. XPS spectra for **a** Ti $2p$ of MCOF-Ti$_6$Cu$_3$, **Ti$_6$** and **b** Cu $2p$ of MCOF-Ti$_6$Cu$_3$, **Cu$_3$**. In-situ XPS spectra of **c** Ti $2p$ and **d** Cu $2p$ for the simulated solar-driven CO_2 reduction process over MCOF-Ti$_6$Cu$_3$. **e** In-situ DRIFTS spectra for the simulated solar-driven CO_2 reduction process over MCOF-Ti$_6$Cu$_3$.

spectroscopy was performed to probe the intermediates[53–58]. As shown in Fig. 4e, new peaks obviously appeared and their intensities gradually increased with the illumination time from 0 to 60 min. The absorption peaks located at 1596, 1578, and 1275 cm^{-1} belong to bidentate carbonate (b-CO_3^{2-}), and the peaks at 1541, 1506, 1473, 1351, and 1330 cm^{-1} are attributed to monodentate carbonate (m-CO_3^{2-}). Additionally, the peaks at 1389 and 1403 cm^{-1} are assigned to polydentate carbonate (p-CO_3^{2-}), and the peaks at 1453, 1434, and 1411 cm^{-1} are ascribed to bicarbonate (HCO$_3^-$). The peak intensities of these carbonates increase significantly, which suggests that MCOF-Ti$_6$Cu$_3$ can chemically adsorb and interact with CO_2 and H_2O molecules. The peak at 1641 cm^{-1} and the emerging peaks at 1742, 1761, and 1775 cm^{-1} maybe result from a formate, and the peak at 1628 cm^{-1} could be attributed to carboxylate. Meanwhile, the intensities of the peaks at 1560, 1526, and 1235 cm^{-1} corresponding to *COOH increased with the prolonged illumination time, which might be possibly caused by the favorable proton capture capability of $CO_2^{\cdot-}$ radicals. Most importantly, the intensity of the peak at 1709 cm^{-1} gradually increased with light progresses[53,57]. This peak is ascribed to *HCOOH which are important intermediates for the formation of HCOOH.

According to the results of in-situ DRIFTS analysis and DFT calculation, the possible mechanism of CO_2 reduction and H_2O oxidation over the hetero-metallic cluster catalyst MCOF-Ti$_6$Cu$_3$ can be reasonably proposed (Fig. 5a). The specific calculation models are in Supplementary Figs. 47, 48 and 49. We conjectured that the Cu cluster unit could be the active site for CO_2 reduction, while the adsorption and activation of H_2O were at the Ti cluster (Fig. 5b). To be specific, under irradiation, the photogenerated electrons and holes separated and transferred to the Cu cluster and Ti cluster, respectively. Then reduction and oxidation reactions took place simultaneously on these two clusters (Fig. 5c). On the Cu cluster, the conversion of CO_2 to HCOOH requires two consecutive hydrogenation steps. The first step is the conversion of CO_2 into *COOH, and then the formed *COOH undergoes a second reaction to generate HCOOH. Correspondingly, the oxidation of H_2O at the Ti cluster involves twice the conversion processes of H_2O into OH•. Finally, when HCOOH is desorbed from the system, the two OH• radicals combine with each other to generate O_2 and H_2O, thus maintaining the charge balance of the catalytic system. As shown in Fig. 5d, the formation of *COOH and OH• from CO_2 and H_2O is the rate determining step in the process of the photocatalytic
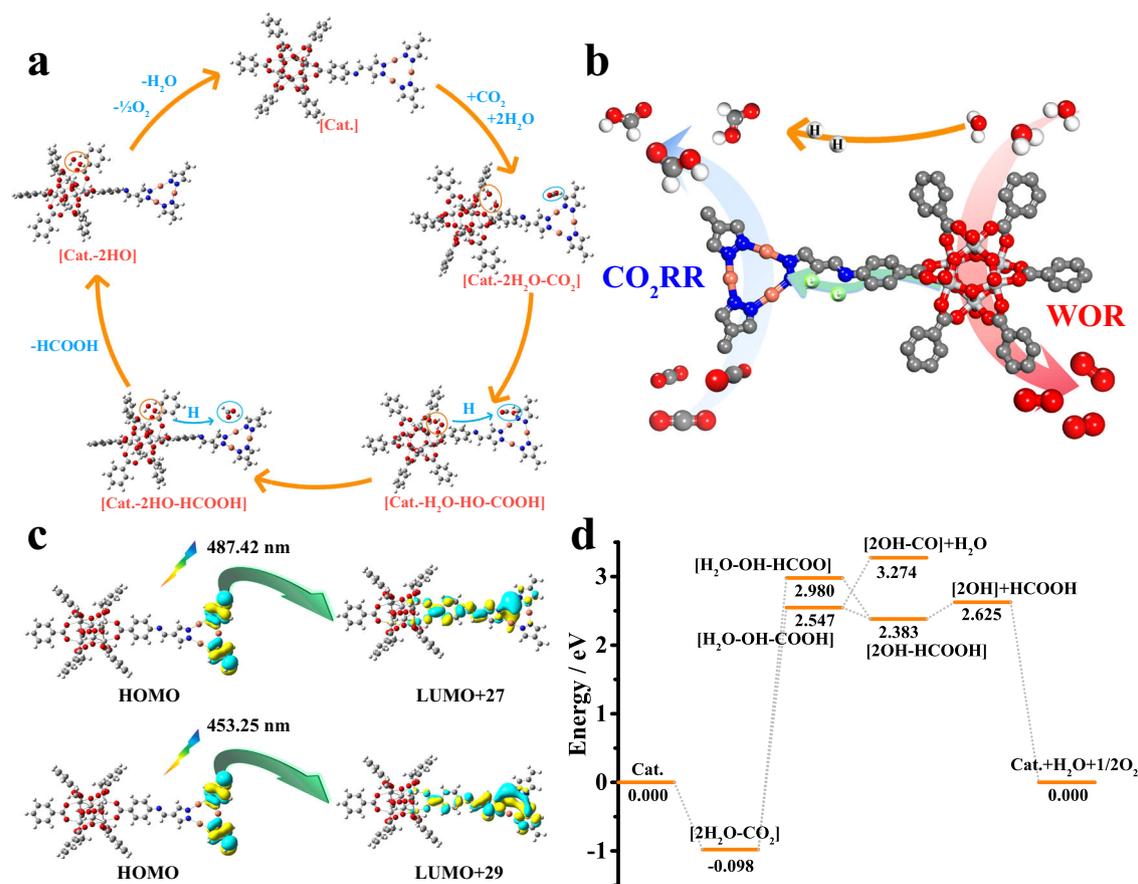
Fig. 5 | Mechanism and DFT calculations. a A proposed reaction pathway for the photocatalytic CO_2 reduction over MCOF-Ti_6Cu_3. **b** Proposed mechanism of CO_2 reduction and H_2O oxidation. **c** Transitions of electron cloud distribution under solar irradiation. **d** Free-energy profile for the CO_2 reduction and H_2O oxidation pathway over MCOF-Ti_6Cu_3.

overall reaction. In addition, two intermediates, *COOH and HCOO*, are generated in the first hydrogenation reaction. The *COOH is preferentially generated since the energy of the formation of *COOH is lower than that of HCOO*. The energy of *COOH dehydration into CO is much higher than that of *COOH hydrogenation into HCOOH, accounting for the preferential generation of HCOOH among the reduction products, which is consistent with the experimental results.

In summary, in order to realize an effective coupled photocatalytic oxidative and reductive overall reaction, we have elaborately designed and constructed a hetero-metallic cluster catalyst via linkage of dynamic covalent bonds, namely MCOF-Ti_6Cu_3, in which functional clusters with reductive and oxidative activities can cooperate for photocatalytic CO_2 reduction and water oxidation, respectively. In addition, hetero-metallic cluster catalyst obtained by directed assembly inherits the oxidative and reductive properties of the clusters and achieves spatial separation. Also, the dynamic covalent bonds have more efficient electron transfer, enabling MCOF-Ti_6Cu_3 to exhibit excellent photocatalytic performance with a high HCOOH yield of 169.8 μmol g^{-1} h^{-1} in crystalline materials with only H_2O. More importantly, the in-situ tests and DFT calculations prove that the reduction reaction occurs on the Cu cluster and the oxidation reaction on the Ti cluster, which is consistent with our pre-designed oxidative and reductive centers on hetero-metallic cluster catalyst, as well as distinctly reveals the charge transfer path and overall photocatalytic reaction mechanism on the atomic level. This research provides a strategy for the construction of hetero-metallic cluster catalyst from the chemical cooperation of MOF ∪ COF, and offers a significant guideline for the design of the photocatalytic overall reaction systems.

Methods

Materials
The starting materials for COF syntheses were purchased from Shanghai Tensus Bio-tech Co., Ltd. Other reagents and solvents applied in the synthesis and photocatalysis were purchased from Aladdin and Sigma-Aldrich, and used as received without further pretreatments.

Synthesis of MCOF-Ti_6Cu_3
Ti_6 (31.1 mg, 0.02 mmol) and Cu_3 (19.8 mg, 0.04 mmol) were mixed in a cylindrical glass tube (20 cm of length, ϕ_{in} = 0.8 cm, ϕ_{out} = 1.0 cm) to which were added mesitylene, DMF and glacial acetic acid (6 M, 9:1:1, $v/v/v$). Then the mixture was sonicated for 15 min to form a homogenous dispersion. After degassed by three freeze-pump-thaw cycles, the tube was sealed off and then heated at 120 °C for 3 days. The bright yellow precipitates (turn green in air) were collected by filtration and soaked in DMF for 24 h. The powder was transferred to a Soxhlet extractor and washed with THF (24 h). Finally, the product was evacuated at 120 °C under vacuum overnight to yield the activated sample.

Photocatalytic experiment
The photocatalytic experiments were carried out following the reported method[45]. In a quartz reactor (50 mL), the catalyst (10 mg) was dispersed in ultra-pure water (30 mL). This mixture system was bubbled with pure CO_2 gas for 20 min. The temperature of the reaction solution was maintained at 25 °C controlled by an outside flow of water during the reaction. Then, the system was irradiated under simulated sunlight using a PLS-SXE300 Xe lamp with an AM 1.5 cut-off filter.

The liquid products in liquid phase of the reactor were measured using ionic chromatography (IC) to analyze HCOOH. The gaseous products were analysed by the gas chromatography. Detailed methods are in the Supplementary Information.

Electrochemical measurements

Photocurrent, electrochemical impedance spectroscopy and Mott-Schottky measurements were all tested using the following methods[45,47]. Electrochemical measurements of MOF901, FDM-71-ABC and MCOF-Ti$_6$Cu$_3$ were tested in a three-electrode electrochemical workstation system (CHI 660e) with the ITO glass substrate (1 cm × 1 cm) as the working electrode, the Pt-wire as the auxiliary electrode and Ag/AgCl electrode as the reference electrode. The samples (2 mg) were dispersed into the solution (1 mL) containing Nafion solution (100 μL, 0.5 wt%), water (450 μL), and ethanol (450 μL). After sonication, the spreading aqueous slurries were drop-cast onto the ITO glass substrate. Then, the working electrode was dried spontaneously under ambient temperature. 0.2 M Na$_2$SO$_4$ solution was used as the electrolyte. Irradiation was carried out by using a 300 W xenon lamp with AM 1.5 cut-off in the photocurrent measurement.

Computational methods

The calculation model is constructed by a finite cluster structure, and all calculations were performed with the Gaussian 16 software package. The ground state of MCOF-Ti$_6$Cu$_3$ was geometrically optimized by using B3LYP method of DFT with Ti, Cu/LanL2dz, C, H, N, O/6-31 G* basis sets[51,52]. ESP analysis, TDDFT calculations, and orbital composition were also performed at the same level. In order to obtain the corresponding excited state energies, TDDFT calculations were performed on the basis of optimized ground state configurations. The energy of [MCOF-Ti$_6$Cu$_3$] is specified as 0.000 eV, and the ΔE (eV) calculations for the other states are shown in Supplementary Tables 6 and 7.

Data availability

The data that support the findings of this study are available within the paper and its supplementary information files or are available from the corresponding authors upon reasonable request. Source data are provided with this paper.

References

1. Jiang, Z. et al. Filling metal-organic framework mesopores with TiO$_2$ for CO$_2$ photoreduction. *Nature* **586**, 549–554 (2020).
2. Lin, S. et al. Covalent organic frameworks comprising cobalt porphyrins for catalytic CO$_2$ reduction in water. *Science* **349**, 1208–1213 (2015).
3. Xu, H. Q. et al. Visible-light photoreduction of CO$_2$ in a metal-organic framework: boosting electron-hole separation via electron trap states. *J. Am. Chem. Soc.* **137**, 13440–13443 (2015).
4. Lin, R.-B. & Chen, B. L. Reducing CO$_2$ with stable covalent organic frameworks. *Joule* **2**, 1030–1032 (2018).
5. Sun, Z. Y. et al. Catalysis of carbon dioxide photoreduction on nanosheets: fundamentals and challenges. *Angew. Chem. Int. Ed.* **57**, 7610–7627 (2018).
6. Zhao, Y. J. et al. Nanoengineering metal-organic framework-based materials for use in electrochemical CO$_2$ reduction reactions. *Small* **17**, 2006590 (2021).
7. Loh, J. Y. Y., Kherani, N. P. & Ozin, G. A. Persistent CO$_2$ photocatalysis for solar fuels in the dark. *Nat. Sustain.* **4**, 466–473 (2021).
8. Shi, Y. et al. Van Der Waals gap-rich BiOCl atomic layers realizing efficient, pure-water CO$_2$-to-CO photocatalysis. *Nat. Commun.* **12**, 5923 (2021).
9. Wang, Q. et al. Molecularly engineered photocatalyst sheet for scalable solar formate production from carbon dioxide and water. *Nat. Energy* **5**, 703–710 (2020).
10. Tachibana, Y. et al. Artificial photosynthesis for solar water-splitting. *Nat. Photonics* **6**, 511–518 (2012).
11. Ye, S. et al. Water oxidation catalysts for artificial photosynthesis. *Adv. Mater.* **31**, 1902069 (2019).
12. Karkas, M. D. et al. Artificial photosynthesis: molecular systems for catalytic water oxidation. *Chem. Rev.* **114**, 11863–12001 (2014).
13. Liu, X., Inagaki, S. & Gong, J. Heterogeneous molecular systems for photocatalytic CO$_2$ reduction with water oxidation. *Angew. Chem. Int. Ed.* **55**, 14924–14950 (2016).
14. Wang, Y. et al. Direct and indirect Z-scheme heterostructure-coupled photosystem enabling cooperation of CO$_2$ reduction and H$_2$O oxidation. *Nat. Commun.* **11**, 3043 (2020).
15. Xu, F. Y. et al. Unique S-scheme heterojunctions in self-assembled TiO$_2$/CsPbBr$_3$ hybrids for CO$_2$ photoreduction. *Nat. Commun.* **11**, 4613 (2020).
16. Sekizawa, K. et al. Artificial Z-scheme constructed with a supramolecular metal complex and semiconductor for the photocatalytic reduction of CO$_2$. *J. Am. Chem. Soc.* **135**, 4596–4599 (2013).
17. Wang, Y. O. et al. Efficient hole trapping in carbon dot/oxygen-modified carbon nitride heterojunction photocatalysts for enhanced methanol production from CO$_2$ under neutral conditions. *Angew. Chem. Int. Ed.* **60**, 20811–20816 (2021).
18. Wang, Z.-W. et al. Cu$^+$-Ti^{3+} interface interaction mediated CO$_2$ coordination model for controlling the selectivity of photocatalytic reduction CO$_2$. *Appl. Catal. B-Environ.* **301**, 120803 (2021).
19. Liu, B. W. et al. Copper-triggered delocalization of bismuth p-orbital favours high-throughput CO$_2$ electroreduction. *Appl. Catal. B-Environ.* **301**, 120781 (2022).
20. Zhuo, T. C. et al. H-bond-mediated selectivity control of formate versus CO during CO$_2$ photoreduction with two cooperative Cu/X sites. *J. Am. Chem. Soc.* **143**, 6114–6122 (2021).
21. Sato, S. et al. Selective CO$_2$ conversion to formate conjugated with H$_2$O oxidation utilizing semiconductor/complex hybrid photocatalysts. *J. Am. Chem. Soc.* **133**, 15240–15243 (2011).
22. Vilela, S. M. F. et al. Multifunctionality in an ion-exchanged porous metal-organic framework. *J. Am. Chem. Soc.* **143**, 1365–1376 (2021).
23. Yusran, Y. et al. Postsynthetic functionalization of covalent organic frameworks. *Natl Sci. Rev.* **7**, 170–190 (2020).
24. Nguyen, H. L. & Alzamly, A. Covalent organic frameworks as emerging platforms for CO$_2$ photoreduction. *ACS Catal.* **11**, 9809–9824 (2021).
25. Li, Z. E. et al. Covalent organic frameworks: pore design and interface engineering. *Acc. Chem. Res.* **53**, 1672–1685 (2020).
26. Xu, H. S. et al. Single crystal of a one-dimensional metallo-covalent organic framework. *Nat. Commun.* **11**, 1434 (2020).
27. Wang, T. X. et al. Central site regulation of cobalt porphyrin conjugated polymer to give highly active and selective CO$_2$ reduction to CO in aqueous solution. *Appl. Catal. B-Environ.* **291**, 120128 (2021).
28. Nguyen, H. L. et al. A titanium-organic framework as an exemplar of combining the chemistry of metal- and covalent-organic frameworks. *J. Am. Chem. Soc.* **138**, 4330–4333 (2016).
29. Xu, W. T. et al. A metal-organic framework of organic vertices and polyoxometalate linkers as a solid-state electrolyte. *J. Am. Chem. Soc.* **141**, 17522–17526 (2019).
30. Wei, R.-J. et al. Copper (I)-organic frameworks for catalysis: networking metal clusters with dynamic covalent chemistry. *CCS Chem.* **3**, 2045–2053 (2021).
31. Zhou, H. G. et al. Acid-triggered interlayer sliding of two-dimensional copper (I)-organic frameworks: more metal sites for catalysis. *Chem. Sci.* **12**, 6280–6286 (2021).
32. Li, X. M. et al. An imine-linked metal-organic framework as a reactive oxygen species generator. *Angew. Chem. Int. Ed.* **60**, 2534–2540 (2020).

33. Elcheikh Mahmoud, M., Audi, H., Assoud, A., Ghaddar, T. H. & Hmadeh, M. Metal-organic framework photocatalyst incorporating *bis*(4'-(4-carboxyphenyl) -terpyridine) ruthenium(II) for visible-light-driven carbon dioxide reduction. *J. Am. Chem. Soc.* **141**, 7115–7121 (2019).

34. Choi, K. M. et al. Plasmon-enhanced photocatalytic CO_2 conversion within metal-organic frameworks under visible light. *J. Am. Chem. Soc.* **139**, 356–362 (2017).

35. Dong, J., Han, X., Liu, Y., Li, H. & Cui, Y. Metal–covalent organic frameworks (MCOFs): a bridge between metal–organic frameworks and covalent organic frameworks. *Angew. Chem. Int. Ed.* **59**, 13722–13733 (2020).

36. Mi, Z. et al. Covalent organic frameworks enabling site isolation of viologen-derived electron-transfer mediators for stable photocatalytic hydrogen evolution. *Angew. Chem. Int. Ed.* **60**, 9642–9649 (2021).

37. Lee, Y. et al. Photocatalytic CO_2 reduction by a mixed metal (Zr/Ti), mixed ligand metal-organic framework under visible light irradiation. *Chem. Commun.* **51**, 5735–5738 (2015).

38. Wang, M. et al. Spatially separating redox centers and photothermal effect synergistically boosting the photocatalytic hydrogen evolution of $ZnIn_2S_4$ nanosheets. *Small* **17**, 2006952 (2021).

39. Yan, Z. H. et al. Photo-generated dinuclear {Eu(II)}$_2$ active sites for selective CO_2 reduction in a photosensitizing metal-organic framework. *Nat. Commun.* **9**, 3353 (2018).

40. Lu, D.-F., Kong, X.-J., Lu, T.-B., Long, L.-S. & Zheng, L.-S. Heterometallic lanthanide–titanium oxo clusters: a new family of water oxidation catalysts. *Inorg. Chem.* **56**, 1057–1060 (2017).

41. Fang, W. H., Zhang, L. & Zhang, J. Synthetic strategies, diverse structures and tuneable properties of polyoxo-titanium clusters. *Chem. Soc. Rev.* **47**, 404–421 (2018).

42. Wang, W. et al. Photocatalytic C–C coupling from carbon dioxide reduction on copper oxide with mixed-valence copper(I)/copper(II). *J. Am. Chem. Soc.* **143**, 2984–2993 (2021).

43. Wu, Y. A. et al. Facet-dependent active sites of a single Cu_2O particle photocatalyst for CO_2 reduction to methanol. *Nat. Energy* **4**, 957–968 (2019).

44. Hong, K. & Chun, H. Nonporous titanium-oxo molecular clusters that reversibly and selectively adsorb carbon dioxide. *Inorg. Chem.* **52**, 9705–9707 (2013).

45. Lu, M. et al. Rational design of crystalline covalent organic frameworks for efficient CO_2 photoreduction with H_2O. *Angew. Chem. Int. Ed.* **58**, 12392–12397 (2019).

46. Li, L. et al. Isoreticular series of two-dimensional covalent organic frameworks with the kgd topology and controllable micropores. *J. Am. Chem. Soc.* **144**, 6475–6482 (2022).

47. Zhang, F.-M. et al. Rational design of MOF/COF hybrid materials for photocatalytic H_2 evolution in the presence of sacrificial electron donors. *Angew. Chem. Int. Ed.* **57**, 12106–12110 (2018).

48. Wang, Y. R. et al. Implanting numerous hydrogen-bonding networks in a Cu-porphyrin-based nanosheet to boost CH_4 selectivity in neutral-media CO_2 electroreduction. *Angew. Chem. Int. Ed.* **60**, 21952–21958 (2021).

49. Dong, L. Z. et al. Stable heterometallic cluster-based organic framework catalysts for artificial photosynthesis. *Angew. Chem. Int. Ed.* **59**, 2659–2663 (2020).

50. Yang, Y. et al. Unexpected "spontaneous" evolution of catalytic, MOF-supported single Cu(II) cations to catalytic, MOF-supported Cu(0) nanoparticles. *J. Am. Chem. Soc.* **142**, 21169–21177 (2020).

51. Wang, J. L. et al. Linking the dynamic chemical state of catalysts with the product profile of electrocatalytic CO_2 reduction. *Angew. Chem. Int. Ed.* **60**, 17254–17267 (2021).

52. Wu, X. Y. et al. Photocatalytic CO_2 conversion of $M_{0.33}WO_3$ sirectly from the air with high selectivity: insight into full spectrum-induced reaction mechanism. *J. Am. Chem. Soc.* **141**, 5267–5274 (2019).

53. Kou, M. P. et al. Photocatalytic CO_2 conversion over single-atom MoN_2 sites of covalent organic framework. *Appl. Catal. B-Environ.* **291**, 120146 (2021).

54. Cao, Y. H. et al. Modulating electron density of vacancy site by single Au atom for effective CO_2 photoreduction. *Nat. Commun.* **12**, 1675 (2021).

55. Xiang, Y. G. et al. Constructing electron delocalization channels in covalent organic frameworks powering CO_2 photoreduction in water. *Appl. Catal. B-Environ.* **274**, 119096 (2020).

56. Wang, B. et al. Sacrificing ionic liquid-assisted anchoring of carbonized polymer dots on perovskite-like $PbBiO_2Br$ for robust CO_2 photoreduction. *Appl. Catal. B-Environ.* **254**, 551–559 (2019).

57. Xi, Y. M. et al. Aspect ratio dependent photocatalytic enhancement of $CsPbBr_3$ in CO_2 reduction with two-dimensional metal organic framework as a cocatalyst. *Appl. Catal. B-Environ.* **297**, 120411 (2021).

58. Gong, S. W. et al. Synergistically boosting highly selective CO_2-to-CO photoreduction over BiOCl nanosheets via in-situ formation of surface defects and non-precious metal nanoparticles. *Appl. Catal. B-Environ.* **297**, 120413 (2021).

Acknowledgements

Author contributions

Y.-Q. L. and J. Z. conceived and designed the idea. J. Z. designed the experiments, collected and analyzed the data. Jie L, L. K., Y. C., and Jia. L. assisted with the experiments and characterizations. J. Z. and Y. Y. analyzed the PXRD data and performed the crystal structure modeling. J. Z. wrote the manuscript. L. Z., Q. H., Y. Y., and S.-L. L. helped with the manuscript revising and data analysis. J. Z. and Y.-Q. L. discussed the results and prepared the manuscript. All the authors reviewed and contributed to this paper.

Competing interests

The authors declare no competing interests.

Additional information

Supplementary information The online version contains supplementary material available at https://doi.org/10.1038/s41467-022-32449-z.

Correspondence and requests for materials should be addressed to Yong Yan or Ya-Qian Lan.

Peer review information *Nature Communications* thanks the anonymous reviewers for their contribution to the peer review of this work.

Reprints and permission information is available at http://www.nature.com/reprints

Publisher's note Springer Nature remains neutral with regard to jurisdictional claims in published maps and institutional affiliations.